doi: 10.82124/CEAS-GNC-2026-064 CEAS-GNC-2026-064

EuroGNC CEAS Madrid, Spain May 5th-7th 2026
uc3m Universidad Carlos III de Madrid AIAA

Simulation and linear-parameter varying control of a large flexible appendage deployment

Andrea Marrazza Research engineer, DYCSYT, Toulouse, France. andrea.marrazza@dycsyt.com

Ervan Kassarian Robust control expert, DYCSYT, Toulouse, France. ervan.kassarian@dycsyt.com

Francesco Sanfedino Associate Professor, Fédération ENAC ISAE-SUPAERO ONERA, Université de Toulouse, Toulouse, France. francesco.sanfedino@isae-supaero.fr

Daniel Alazard Professor, Fédération ENAC ISAE-SUPAERO ONERA, Université de Toulouse, Toulouse, France. daniel.alazard@isae-supaero.fr

Diego Navarro-Tapia Senior Research Associate, Universidad Carlos III de Madrid (UC3M), Spain. diego.navarro.tapia@uc3m.es

Andrés Marcos Depart. Aerospace Engineering, Universidad Carlos III de Madrid (UC3M), Spain. anmarcos@ing.uc3m.es

Joost Veenman Robust control systems expert, SENER Aerospacial, Spain. joost.veenman.external@aeroespacial.sener

ABSTRACT

This work investigates a Linear Parameter Varying (LPV) control framework that enables continuous satellite attitude control during deployment of large flexible appendages, scheduled by hinge angles. An LPV model of the satellite is derived in the Linear Fractional Transformation framework based on a multibody approach, and validated against a high-fidelity `Simscape` nonlinear model. Two LPV controllers are then designed and compared: an analytical PD-based controller, which continuously adapts gains to the time-varying inertia and maintains attitude control throughout the entire deployment sequence; and a robust $\mathcal{H}_\infty$ LPV controller, designed for the first deployment phase, which demonstrates improved pointing performance over the analytical baseline. Simulation results confirm the effectiveness of the proposed modeling and control approach, highlighting its potential to improve both performance and operational simplicity in future missions.

Keywords: LPV control, deployment, large flexible appendages, robust control, spacecraft

Nomenclature

A calligraphic letter (for example $\mathcal{B}$) is used to label a rigid body. The same uppercase letter (B) is used to denote its center of mass (CoM). The subscript with the same lower case letter (b) is used to denote its body frame and reference axes (for example, $\mathcal{R}_b = (O, \mathbf{x}_b, \mathbf{y}_b, \mathbf{z}_b)$ is the body frame attached to $\mathcal{B}$ at the reference point O). In addition, the following notations will be used throughout this paper:

$\overrightarrow{PC}$	The vector from point P to point C (3×1 vector, m).
$\mathbf{P}_{a/b}$	3×3 Direction Cosine Matrix (DCM) of the rotation from frame $\mathcal{R}_a$ to frame $\mathcal{R}_b$, that contains the coordinates of vectors $\mathbf{x}_a$, $\mathbf{y}_a$, $\mathbf{z}_a$ expressed in frame $\mathcal{R}_b$.
$\boldsymbol{\omega}^{\mathcal{B}}$	Angular speed of $\mathcal{R}_b$ with respect to $\mathcal{R}_i$ (3×1 vector, rad/s).
$\mathbf{a}_P^{\mathcal{B}}$	Inertial acceleration of body $\mathcal{B}$ at point P (3×1 vector, m/s^2).
$\mathbf{F}_{\mathcal{B}/\mathcal{A}}$	Force applied by body $\mathcal{B}$ on body $\mathcal{A}$ (3×1 vector, N).
$\mathbf{T}_{\mathcal{B}/\mathcal{A},P}$	Torque applied by $\mathcal{B}$ on $\mathcal{A}$ at point P (3×1 vector, Nm).
$[\star]_{\mathcal{R}_b}$	Projection of $\star$ (vector, wrench, tensor, model,...) in the frame $\mathcal{R}_b$. For a vector $\mathbf{v}$: $[\mathbf{v}]_{\mathcal{R}_b} = \mathbf{P}_{a/b}[\mathbf{v}]_{\mathcal{R}_a}$.
$\mathbf{W}_{\mathcal{B}/\mathcal{A},P}$	6×1 wrench applied by $\mathcal{B}$ on $\mathcal{A}$ at point P: $\mathbf{W}_{\mathcal{B}/\mathcal{A},P} = \begin{bmatrix} \mathbf{F}_{\mathcal{B}/\mathcal{A}} \\ \mathbf{T}_{\mathcal{B}/\mathcal{A},P} \end{bmatrix}$.
$\mathbf{W}_{./\mathcal{A},P}$	6×1 local wrench applied on $\mathcal{A}$ at point P.
$\mathbf{W}_{\mathcal{A}/.,P}$	6×1 local wrench applied by $\mathcal{A}$ at point P.
$\ddot{\mathbf{u}}_P^{\mathcal{B}}$	6×1 acceleration dual vector of body $\mathcal{B}$ at point P: $\mathbf{x}''^{\mathcal{B}}_P = \begin{bmatrix} \mathbf{a}_P^{\mathcal{B}} \\ \dot{\boldsymbol{\omega}}^{\mathcal{B}} \end{bmatrix}$.
$\mathbf{P}^{\times 2}_{a/b}$	Augmented DCM for dual vectors $\mathbf{P}^{\times 2}_{a/b} = \mathrm{diag}\left(\mathbf{P}_{a/b}, \mathbf{P}_{a/b}\right)$.
$\mathbf{D}^{\mathcal{A}}_P(\mathrm{s})$	6×6 dynamic model of body $\mathcal{A}$ expressed at point P.
$\mathbf{D}^{\mathcal{A}}_{PC}(\mathrm{s})$	12×12 TITOP dynamic model of body $\mathcal{A}$ expressed at points P and C.
s	Laplace variable.
$\mathbf{0}_{n \times m}$	Zero matrix $n \times m$.

1 Introduction

Current and future Earth observation missions increasingly rely on spacecraft equipped with very large deployable appendages. These structures introduce low-frequency flexible modes and involve complex deployment scenarios during which the need to protect the fragile deployment hinges significantly limits the Attitude and Orbit Control System (AOCS) in rejecting orbital disturbances and maintaining pointing accuracy. Current AOCS strategies [1], however, present several limitations that directly affect mission performance and operational complexity.

First, during deployment, attitude control is traditionally deactivated at each step and re-enabled only after completion of the maneuver to recover sun-pointing with the required accuracy. This procedure relies on two successive control modes: a low-bandwidth safe mode, designed to guarantee stability even in failure scenarios and to minimize torque applied to the hinges, followed by a higher-bandwidth nominal mode to restore pointing accuracy. The consequences of this approach are threefold: (i) long re-pointing durations at the end of each deployment step; (ii) a demanding design and validation process, since the number of control modes scales with the number of configurations and each must remain robust to partial deployment; and (iii) increased operational complexity, as ground teams must update AOCS control parameters after each step.

Second, the safe mode generally relies on B-dot control using magnetorquers. Owing to their inherently limited torque capacity, magnetorquers cannot damage the hinges even in the case of latching failure. Moreover, this control strategy, which provides a dissipative torque and passively aligns the spacecraft with the orbital normal, is robust to a wide range of inertias, including partial deployments. While simple and reliable, this approach significantly increases re-pointing times, especially in the presence of large gravity-gradient torques and atmospheric drag generated by the deployed appendages.

To address these limitations, and in particular to reduce deployment duration—which is critical for collision avoidance—as well as to simplify design and operations, this study investigates linear parameter varying (LPV) control, with the following objectives:

- maintain pointing precision during deployment by enabling control throughout the process, scheduled with hinge angles;
- reduce design and validation effort by tuning only a limited set of time-varying controllers applicable across all deployment steps;
- minimize reliance on ground updates of AOCS parameters.

To do so, accurate linearized plants are needed along the trajectory, hence the system is modeled with a multi-body approach implemented in the Satellite Dynamics Toolbox Library (SDTlib).

The `SDTlib` [2, 3] is based on the TITOP (Two-Input Two-Output Ports) modeling approach [4], which allows the system to be assembled from the models of its mechanical subcomponents and enables the derivation of a Linear Fractional Transformation (LFT) that captures all parametric variations and uncertainties within a single plant model. This representation is formulated at the subsystem level directly from the governing physical equations, without requiring interpolation or other approximations beyond linearity.

This approach has been successfully applied to address complex control–structure interaction problems, such as control/structure co-design [5], line-of-sight control [6], or propagation of microvibrations induced by onboard mechanisms [7]. A particularly relevant reference to the present work is [8], where the LFT framework was employed to model the robotic manipulation of a client spacecraft by a servicer spacecraft and to design a robust controller capable of handling large variations in inertia and flexible modes.

The resulting model can be used for LPV simulations that reproduce the nonlinear system behavior with significantly reduced computational cost, by employing linear formulations whose parameters vary to reflect some of the underlying nonlinear dynamics. Moreover, it integrates directly with the MATLAB Robust Control Toolbox to perform robust LPV control via standard $\mathcal{H}_\infty$ methods, ensuring accurate reference tracking while limiting loads on fragile mechanisms.

2 Modelling of the spacecraft with SDTlib

2.1 Basics on TITOP modelling approach

2.1.1 Model of a flexible body

Let us consider a flexible body $\mathcal{A}$ as seen in Fig. 1 (left) connected to a parent structure $\mathcal{P}$ at the point P and to a child structure C at the point C. The resulting TITOP model $\mathbf{D}^{\mathcal{A}}_{PC}(\mathrm{s})$, schematized in Fig. 1 (right), is a 12×12 linear dynamic model whose inputs are:

- $\mathbf{W}_{C/\mathcal{A},C}$: the 6×1 wrench (forces and torques) applied by the body C to $\mathcal{A}$ at point C;
- $\ddot{\mathbf{u}}^{\mathcal{A}}_{P}$: the 6×1 inertial acceleration (linear and angular) imposed by the parent body $\mathcal{P}$ at point P to $\mathcal{A}$;

and the conjugated outputs are:

- $\ddot{\mathbf{u}}_{C}$: the 6×1 components of the inertial acceleration of point C;
- $\mathbf{W}_{\mathcal{A}/\mathcal{P},P}$: the 6×1 wrench applied by $\mathcal{A}$ to the parent structure $\mathcal{P}$ at point P.

All these input/output variables are projected in the body frame $\mathcal{R}_a$.

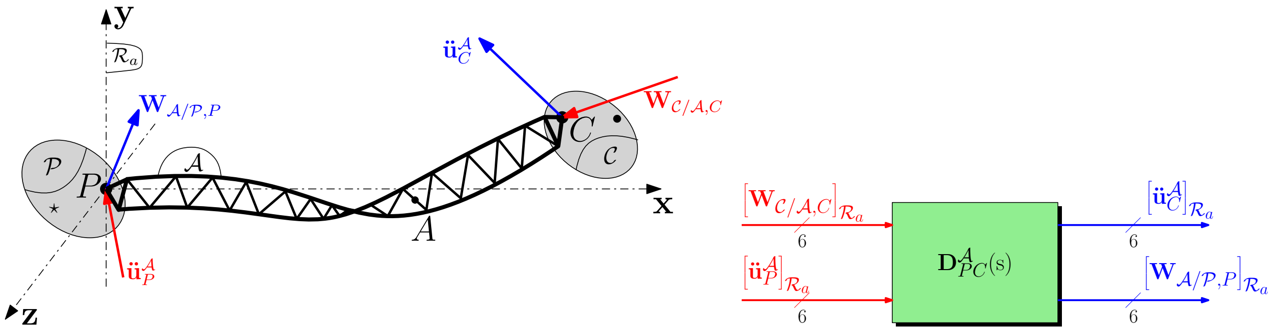

Fig. 1 TITOP scheme and nomenclature for a generic flexible appendage $\mathcal{A}$.

As described in [4], the state-space representation of $\mathbf{D}_{PC}^{\mathcal{A}}(\mathrm{s})$ can be directly built from the mechanical parameters of the body $\mathcal{A}$:

$$\left[\begin{array}{c} \dot{\boldsymbol{\eta}} \\ \ddot{\boldsymbol{\eta}} \\ \hline \ddot{u}_C \\ \mathbf{W}_{P/} \end{array}\right] = \left[\begin{array}{cc|cc} \mathbf{0}_{n\times n} & \mathbf{I}_n & \mathbf{0}_{n\times 6} & \mathbf{0}_{n\times 6} \\ -\mathrm{diag}(\omega_j^2) & -\mathrm{diag}(2\xi_j\omega_j) & \mathbf{\Phi}_C^T & -\mathbf{L}_P \\ \hline -\mathbf{\Phi}_C\,\mathrm{diag}(\omega_j^2) & -\mathbf{\Phi}_C\,\mathrm{diag}(2\xi_j\omega_j) & \mathbf{\Phi}_C\mathbf{\Phi}_C^T & (\tau_{CP}-\mathbf{\Phi}_C\mathbf{L}_P) \\ \mathbf{L}_P^T\,\mathrm{diag}(\omega_j^2) & \mathbf{L}_P^T\,\mathrm{diag}(2\xi_j\omega_j) & (\tau_{CP}-\mathbf{\Phi}_C\mathbf{L}_P)^T & -\mathbf{D}_P+\mathbf{L}_P^T\mathbf{L}_P \end{array}\right] \left[\begin{array}{c} \boldsymbol{\eta} \\ \dot{\boldsymbol{\eta}} \\ \hline \mathbf{W}_{/C} \\ \ddot{u}_P \end{array}\right] \qquad (1)$$

where:

- n is the number of flexible clamped-free modes of the body $\mathcal{A}$ characterized by the modal coordinates vector $\boldsymbol{\eta}$, the frequencies ω_j, $j = 1,\dots,n$ and the damping ratio ξ_j, $j = 1,\dots,n$,
- $\mathbf{I}_n$ is the identity matrix of size n,
- $\mathbf{L}_P$ is the $n \times 6$ modal participation factor matrix of the body at point P,
- $\mathbf{\Phi}_C$ is the $6 \times n$ projection matrix of the n clamped-free modal shapes on the 6 d.o.f.s at point C,
- τ_{CP} is the "rigid" kinematic model between point C and P:

$$\tau_{CP} = \begin{bmatrix} \mathbf{I}_3 & ({}^*\overrightarrow{CP}) \\ \mathbf{0}_{3\times 3} & \mathbf{I}_3 \end{bmatrix}$$

  where $({}^*\overrightarrow{CP})$ is the skew-symmetric matrix associated to the vector from C to P,
- $\mathbf{D}_P$ is the total 6×6 rigid mass matrix of the body at point P.

(In the SDTlib, these data can be picked-up in the NASTRAN output files of the body $\mathcal{A}$ when it is clamped at P and free at C (through a NASTRAN/SIMULINK interface) or derived analytically for simple shaped body (beams and plates)).

In the case where the body $\mathcal{A}$ presents parametric uncertainties (on mass, inertia, flexible modes, etc.) collected in the vector $\boldsymbol{\delta} = (\delta_1,\dots,\delta_n)$, the system $\mathbf{D}_{PC}^{\mathcal{A}}(s,\boldsymbol{\delta})$ can be represented by a LFT, as shown in Fig. 2.

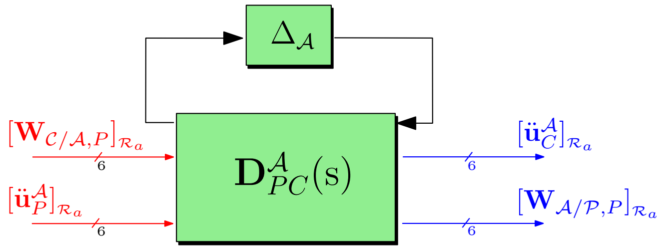

Fig. 2 LFT scheme for a generic flexible appendage $\mathcal{A}$ with uncertain parameters. The nominal system is denoted by $\mathbf{D}^{\mathcal{A}}_{PC}(s)$, and the uncertainty block $\Delta_{\mathcal{A}}$ is a block-diagonal matrix defined as $\Delta_{\mathcal{A}} = \mathrm{diag}(\delta_1 I_{q_1}, \ldots, \delta_n I_{q_n})$, where q_i represents the number of repetition of the uncertainty δ_i in the system.

2.1.2 Multibody modelling

Then the model of the assembly of this body $\mathcal{A}$, the parent body $\mathcal{P}$ (itself connected at the point $\star$ to another body) and the child body C (itself connected at the point $\bullet$ to another body) is performed by the feedback inter-connections of the TITOP models of the various elements through the DCMs (Direct Cosine Matrices) between the body frames.

When each body is represented in LFT form, the resulting overall model corresponds to the nominal overall model with a feedback interconnection involving a block-diagonal matrix composed of the individual uncertainty blocks of each body, as shown in Fig. 3.

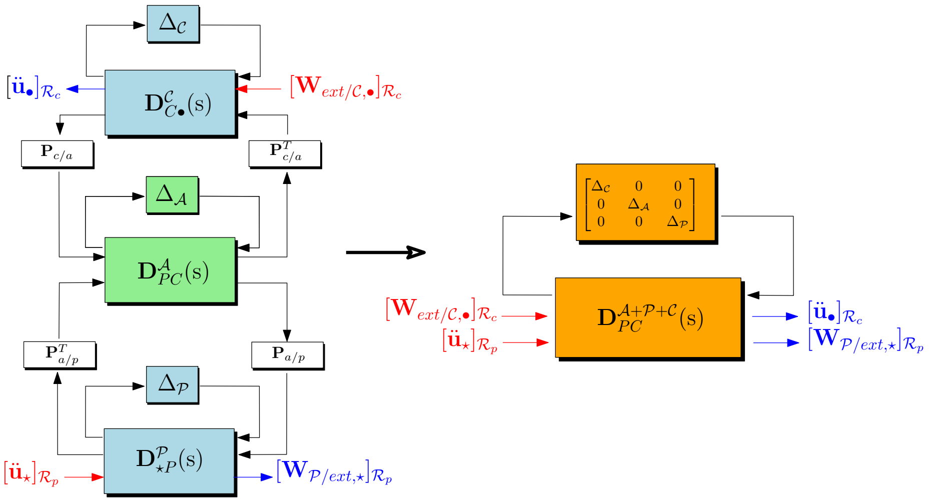

Fig. 3 TITOP model of the assembly in LFT form.

When the bodies $\mathcal{P}$ and $\mathcal{A}$ are connected through a revolute joint with a time-varying configuration θ, the DCM $\mathbf{P}_{a/p}(\theta)$, which now depends on θ, can be expressed as an LFT involving the new parametrization $\sigma = \tan(\theta/4)$ [9] and thus be included in the LPV model of the system (σ is then considered as a varying parameter; not as a state variable). Finally the TITOP model of the revolute joint includes also an additional SISO (Single Input Single-Output) channel between the torque applied inside the revolute joint by a local actuator (e.g. for instance the Solar Aray Drive Mechanism (SADM)) and the in-joint angular acceleration $\ddot{\theta}$ (assumed to be small to satisfy the linearity assumption). This channel can be used to take into account a model of the local mechanism.

Fig. 4 shows the TITOP model of the revolute joint, where:

- $[\mathbf{W}_{./r_{out},P}]_{\mathcal{R}_j}$: external wrench applied to the output shaft by the child body at point P, expressed in joint frame $\mathcal{R}_j$,
- $[\ddot{\mathbf{u}}_{in}]_{\mathcal{R}_j}$: acceleration twist of the input shaft at point P, expressed in $\mathcal{R}_j$,
- C_m: driving torque applied inside the revolute joint by the input shaft to the output shaft,
- $[\ddot{\mathbf{u}}_{out}]_{\mathcal{R}_j}$: acceleration twist of the output shaft at point P, expressed in $\mathcal{R}_j$,
- $[\mathbf{W}_{r_{in}/.,P}]_{\mathcal{R}_j}$: wrench applied by the input shaft on the parent body at point P, expressed in $\mathcal{R}_j$,
- $\ddot{\theta}$: relative angular acceleration of the output shaft with respect to the input shaft.

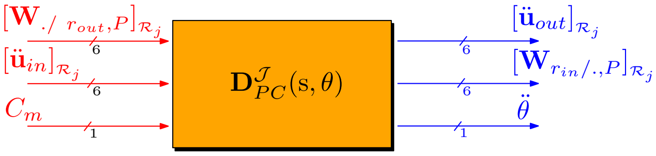

Fig. 4 **Revolute Joint TITOP scheme**

2.2 Model of a spacecraft with a Large Deployable Reflector (LDR)

2.2.1 Overview of the spacecraft

The system considered for LPV control is a satellite equipped with a solar panel and a large deployable reflector, as shown in Fig. 5a. Both the model and the data used for its development are inspired by the BIOMASS mission [1, 10]. As introduced in Sec. 1 and further detailed in this section, the model is derived using the `SDTlib`, which enables the construction of an LPV model that integrates all the kinematic and dynamic submodels of the booms, ribs, and hinges involved in the Large Deployable Reflector (LDR).

The resulting model is fully parameterized with respect to the geometric configurations of the various hinges and is validated by comparison with the SIMSCAPE non-linear model when it is linearized on a grid of geometric configurations. It is worth emphasizing the novelty of this approach with respect to the more classical ones. Traditionally, LPV models are built by interpolating among a set of linear models, each obtained through simplification and linearization of the full non-linear validation model sampled on a grid of the varying parameters. Thus with no guaranty on the correctness of the interpolated model between 2 points of the grid. In contrast, the proposed sub-structuring approach ensures model correctness for any geometric configuration of the substructures. Moreover, it allows direct computation of the interaction wrenches between substructures, enabling the monitoring of hinge loads during deployment.

Figure 5 presents both a 3D view and a schematic representation of the spacecraft architecture with the LDR in its fully deployed configuration. In the figure, the reflector is depicted together with the membrane forming the reflective surface; however, for simplicity, the `SDTlib` model includes only the structural beams composing the umbrella framework that supports the membrane.

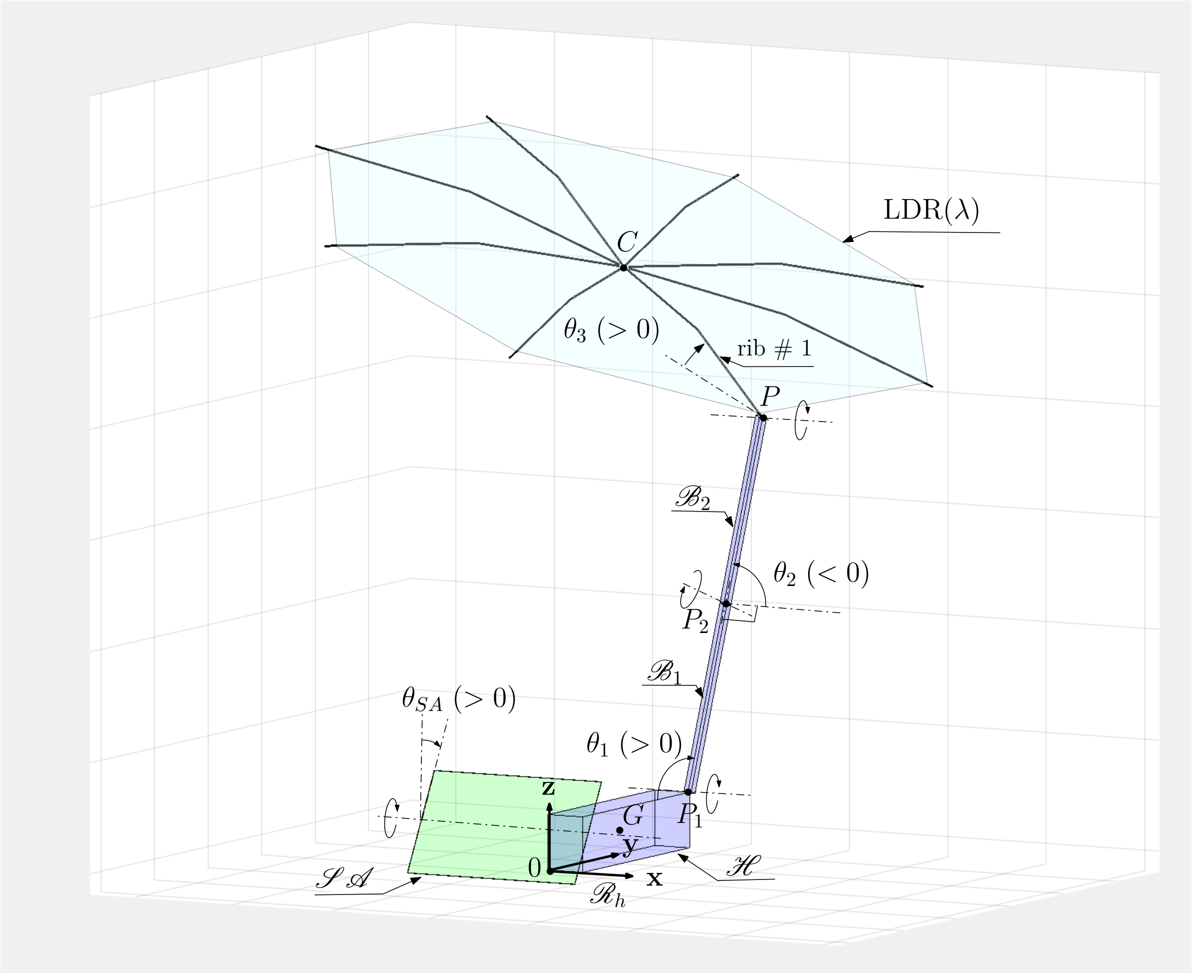

(a) Full satellite with deployed LDR 3D visualization

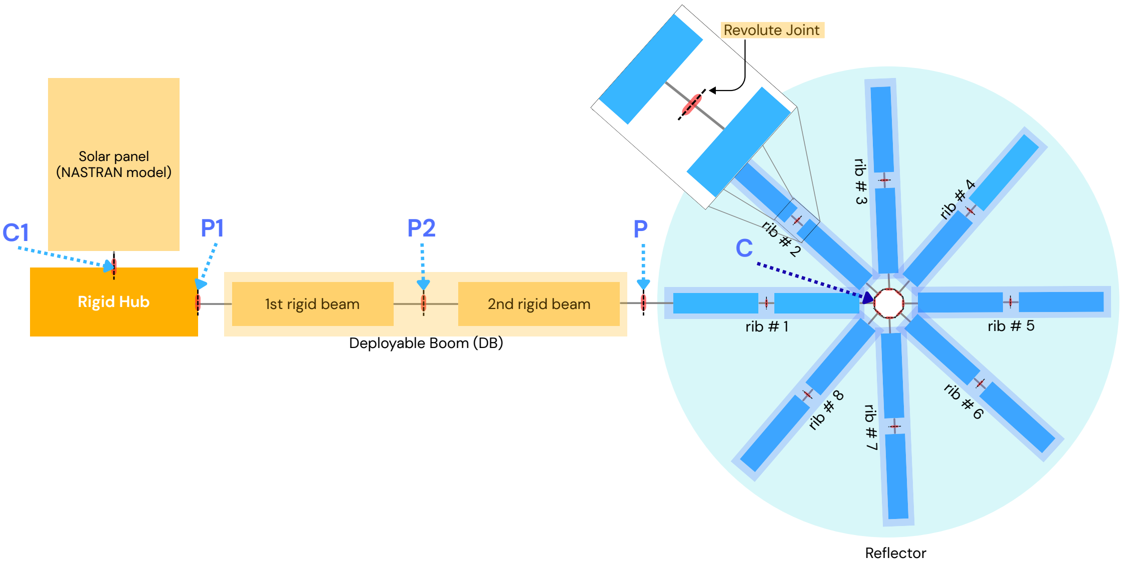

(b) Full satellite with deployed LDR functional scheme

Fig. 5 Satellite with rotating solar array and a LDR: (a) realistic 3D visualization , (b) functional scheme

As shown in Fig. 5a and 5b, the reflector is connected to the main body $\mathscr{H}$ through the Deployable Boom (DB) composed of two flexible booms $\mathscr{B}_1$ and $\mathscr{B}_2$ and three hinges with angular configurations θ_1,

θ_2 and θ_3 located at points P_1, P_2 and P. The angular parametrization $(\theta_1, \theta_2, \theta_3)$ is defined so that the variation bounds between the stowed and deployed configurations never include π or $-\pi$. For instance, if $\theta_1 \in [\pi/2,\ 3\pi/2]$, we define

$$\theta_1 = \pi + \tilde{\theta}_1, \quad \text{with } \tilde{\theta}_1 \in [-\pi/2,\ \pi/2],$$

and the corresponding uncertain parameter becomes

$$\sigma_1 = \tan\left(\frac{\tilde{\theta}_1}{2}\right).$$

This approach allows the use of the parametrization $\sigma_i = \tan(\tilde{\theta}_i/2)$, $i = 1, 2, 3$, leading to a LFT with fewer parametric occurrences (8 instead of 16) compared with the $\theta_i/4$ parametrization.

A 6.8 m^2 flexible solar array $\mathcal{S}_A$, modelled in PATRAN/NASTRAN, is connected to the main body at point C_1 along the $-x$ axis of the spacecraft reference body frame and can be tilted by an angle θ_{SA} around x. The classical parametrization is used for the angular configuration of the solar array $\mathcal{S}_A$, which can vary between $-\pi$ and π: $\sigma_{\mathcal{SA}} = \tan\left(\frac{\theta_{SA}}{4}\right)$.

2.2.2 *Model of the LDR*

The 12 m diameter LDR is composed of an umbrella-like reflector composed of 8 ribs. Each ribs is composed of 2 rigid (3 meters long) beams connected to each other with flexible hinges that act as revolute joints exhibiting inherent stiffness and damping properties. The connection point P between the LDR and the deployable boom (DB) corresponds to the free tip of one rib (denoted as rib #1, see Fig. 5).

The model of the LDR is fully parametrized according to a deployment configuration parameter λ that can vary between 0 and 1, scheduling simultaneously the angular configurations of all rib hinges forming the reflector. :

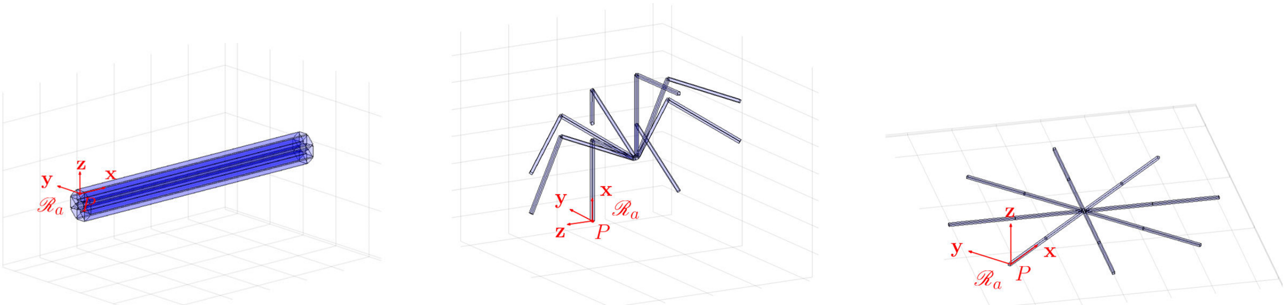

(a) $\lambda = 0$: Reflector stowed **(b) $\lambda = 0.5$: Reflector half deployed** **(c) $\lambda = 1$: Reflector fully deployed**

Fig. 6 Reflector deployment configurations for different values of λ.

The reflector is then connected to the 2 beams forming the DB (as in Fig 5) to obtain the LDR dynamic model at point P_1: $\mathcal{D}_{P_1}^{\mathcal{LDR}}(s, \mathbf{\Theta}_{\mathcal{LDR}})$. All the required interconnections follow the TITOP formalism explained in Section 2.1.

2.2.3 *Model of the spacecraft and deployment*

Figure. 7 illustrates the TITOP schematic of the complete satellite system. In this representation, $\mathcal{D}_{P_1C_1}^{\mathcal{H}}(s)$ denotes the dynamic model of the main hub, $\mathcal{D}_{C_1}^{\mathcal{SA}}(s, \sigma_{\mathcal{SA}})$ represents the LFT model of the solar array, and $\mathcal{D}_{P_1}^{\mathcal{LDR}}(s, \mathbf{\Theta}_{\mathcal{LDR}})$ corresponds to the LFT model of the LDR plus deployment boom (DB).

The parameter vector $\mathbf{\Theta}_{\mathcal{LDR}}$ captures the varying angular configurations of the hinges in the DB and LDR, expressed as

$$\mathbf{\Theta}_{\mathcal{LDR}} = \left[\lambda, \quad \tan\left(\frac{\theta_1}{2}\right), \quad \tan\left(\frac{\theta_2}{2}\right), \quad \tan\left(\frac{\theta_3}{2}\right)\right].$$

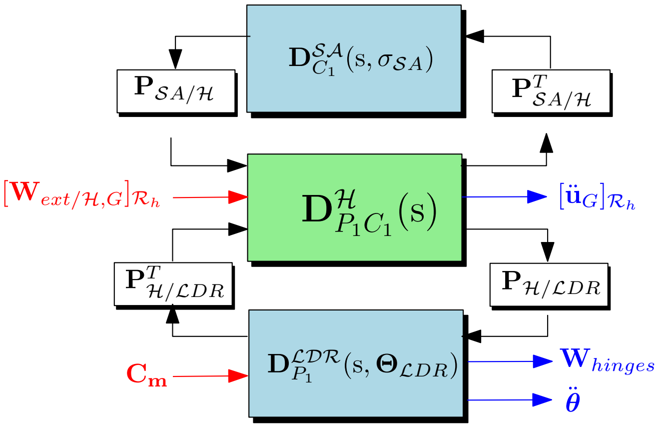

Fig. 7 TITOP scheme of the full BIOMASS satellite

The resulting model $\mathbf{D}_G(s, \mathbf{\Theta})$ of the whole spacecraft is thus parametrized according to the geometric configuration vector:

$$\mathbf{\Theta} = \left[\lambda, \quad \tan(\theta_1/2), \quad \tan(\theta_2/2), \quad \tan(\theta_3/2), \quad \tan(\theta_{SA}/4)\right]^T.$$

As visible in Fig. 7, the system consists of the following inputs:

- $[\mathbf{W}_{ext/\mathcal{H},G}]_{\mathcal{R}_h}$: the 6×1 input wrench vector applied on the main body $\mathcal{H}$ at point G (a reference point on the main body; for instance its centre of mass) and projected in the main body frame $\mathcal{R}_h$. This wrench includes the orbital disturbances (forces and torques) and the force and torque due to the AOCS (Attitude and Orbit Control System).
- $\mathbf{C_m}$: the 4×1 input torque vector at some particular hinges:
    - at P_1: the hinge between the main body and the first boom (and projected in the frame $\mathcal{R}_{b_1}$),
    - at P_2: the hinge between the 2 booms (and projected in the frame $\mathcal{R}_{b_2}$),
    - at P: the hinge between the boom $\mathcal{B}_2$ and the LDR (and projected in the frame $\mathcal{R}_a$),
    - at C: the hinge at the tip of the rib #1, holding the other ribs (and projected in the frame $\mathcal{R}_a$).

and the following outputs:

- $[\ddot{\mathbf{u}}_G]_{\mathcal{R}_h}$: the 6×1 output vector of the inertial acceleration at point G and projected in the main body frame $\mathcal{R}_h$,
- $\mathbf{W}_{hinges}$: the 24×1 output vector of the wrenches acting on the 4 hinges at P_1, P_2, P, C (6 wrenches per hinge),
- $\ddot{\boldsymbol{\theta}}$: the 4×1 angular acceleration vector of said particular hinges.

Table 1 summarizes the ranges of variation of each geometric configuration parameter, its values for the stowed and deployed configurations and the direction of the hinge axis with respect to the main body frame $\mathscr{R}_b = (0, x, y, z)$, while Fig. 8 shows the various configurations during deployment.

parameter	range	stowed value	deployed value	description
θ_{SA}	$[-\pi,\, \pi]$	–	–	around x-axis
θ_1	$\left[0,\, 5\pi/8\right]$	0	$5\pi/8$	around x-axis
θ_2	$\left[-\pi/2,\, \pi/2\right]$	$\pi/2$	$-\pi/2$	around z-axis when $\theta_1 = 0$
θ_3	$\left[-\pi/2,\, \pi/2\right]$	$-\pi/2$	$\pi/12$	around x-axis when $\theta_2 = 0$
λ	$\left[0,\, 1\right]$	0	1	the 16 umbrella hinges

Table 1 Ranges of variation of the geometric configuration parameters.

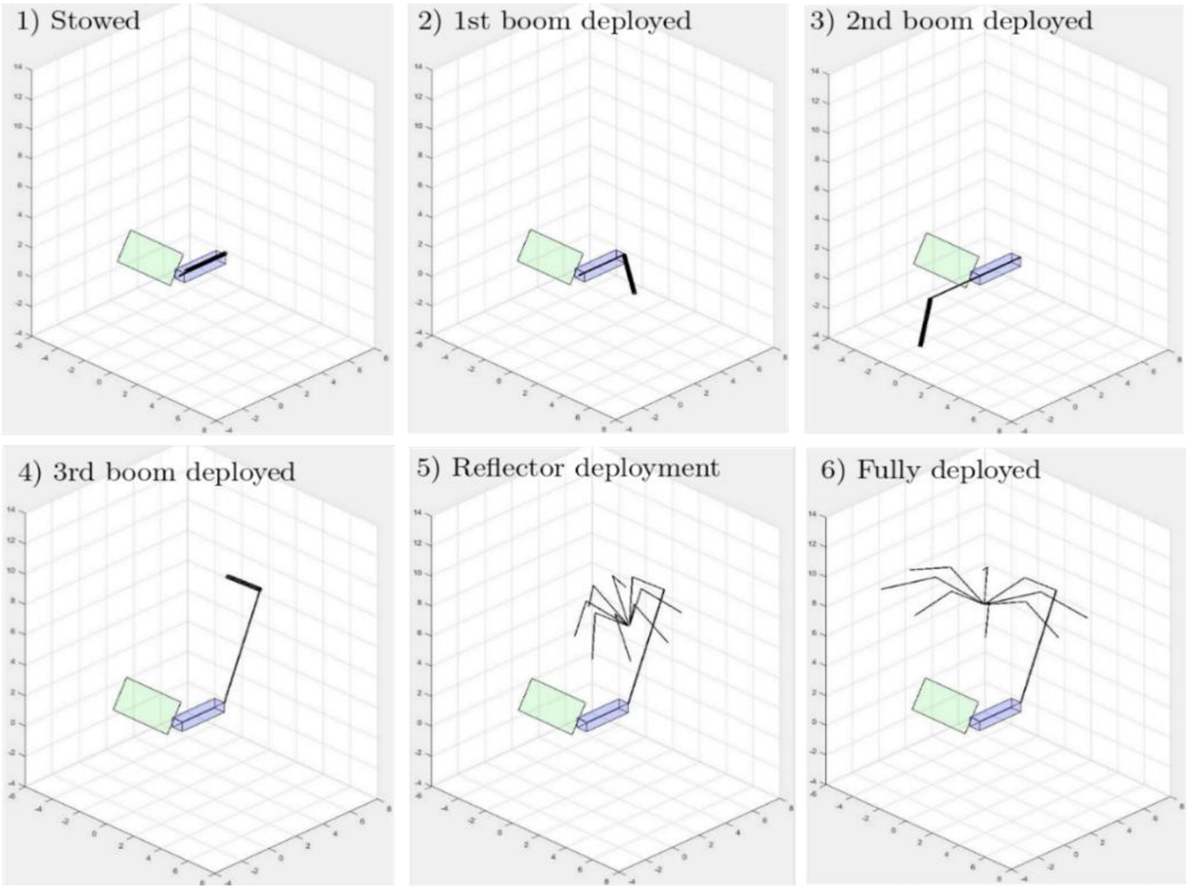

Fig. 8 Deployment of the DB + LDR:
1) Fully stowed,
2) Rib #1 deployed ($\theta_3 = \pi/12$)**,**
3) 2$^{\mathbf{nd}}$ **rigid beam of DB deployed** ($\theta_2 = -\pi/2$)**,**
4) 1$^{\mathbf{st}}$ **rigid beam of DB deployed** ($\theta_1 = 5\pi/8$)**,**
5) Reflector deployment ($\lambda = 0.5$)**,**
6) Fully deployed ($\lambda = 1$)

3 Model validation and preliminary deployment analysis

3.1 Preliminary deployment analysis

The SDTlib model of the spacecraft just described allows for a preliminary analysis of the satellite dynamics during deployment of the DB and LDR. For example, Fig.9 illustrates the evolution of the satellite inertia along the X, Y, and Z axes in the main body frame $\mathcal{R}_h$ during antenna deployment. The configurations are sampled from the LFT model at different points of the deployment (the abscissa should be considered as the evolution of these points rather than a time scale, as it does not account for pauses between deployment steps for example). As shown, the change in inertia from the stowed to the fully deployed configuration is substantial, and particularly along the X and Y axes, where the final values are nearly 20 times greater than the initial ones, consistent with those reported in [1] for BIOMASS.

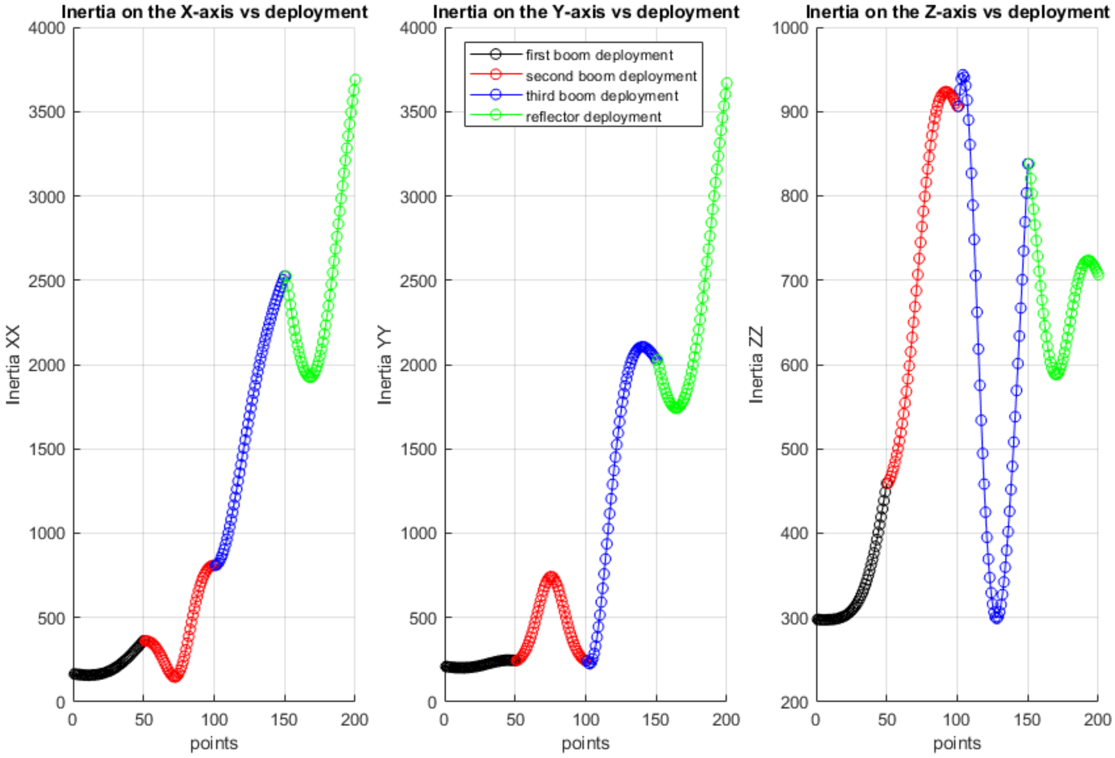

Fig. 9 Variation of moments of inertia during deployment

As previously noted, the hinges exhibit inherent stiffness and damping properties. To account for the effect of the latching mechanisms, the stiffness of each hinge is governed by a Boolean parameter Λ_i, which can take values of 0 or 1 (this parameter is used in simulation, but it is not treated as an uncertain parameter) . When the i-th joint is latched ($\Lambda_i = 1$), its stiffness is set to 15,000 Nm/rad [10]. When the latching mechanism is disengaged ($\Lambda_i = 0$), the joint stiffness is reduced to $1/100$ of its latched value, representing the residual natural stiffness present during deployment. For the i-th joint:

$$K_p^i = \begin{cases} 15000 \text{ Nm/rad}, & \text{if } \Lambda_i = 1 \text{ (latched)} \\ 150 \text{ Nm/rad}, & \text{if } \Lambda_i = 0 \text{ (unlatched)} \end{cases} \tag{2}$$

Under this stiffness model, Fig. 10 illustrates the behavior of the first-mode frequencies. These frequencies are dominated by the hinge stiffness, as the modes associated with the solar arrays occur at much higher frequencies and are therefore less critical from a control perspective.

A deployment step starts with a release of the hinge and ends with latching, resulting in much lower frequencies during the boom deployment steps than in-between. Thus, this model can be used both for safe and nominal modes. The minimum frequency observed was 0.67 rad/s, occurring during the deployment of the third boom.

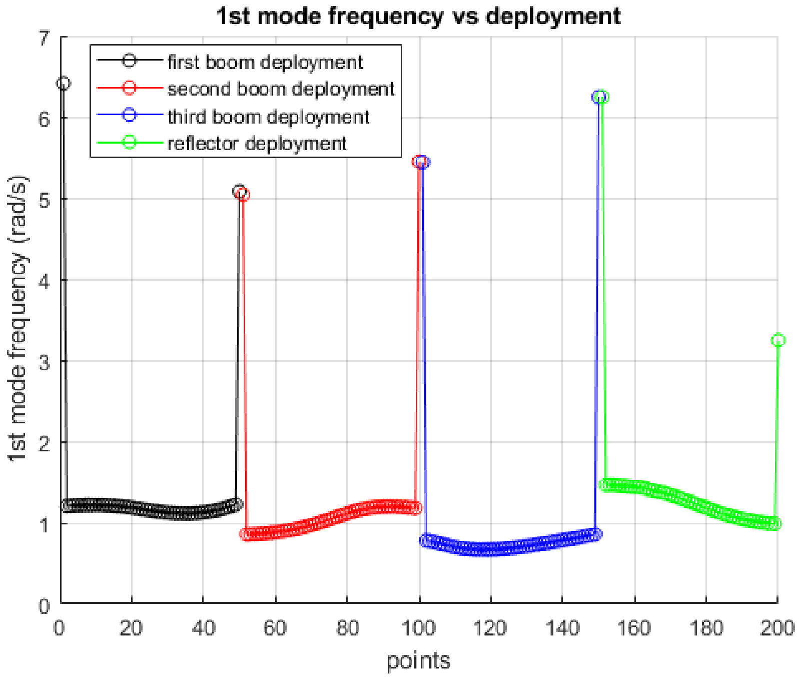

Fig. 10 Evolution of the first flexible mode frequency during deployment

3.2 Comparison with SIMSCAPE-MULTIBODY

The MATLAB toolbox SIMSCAPE-MULTIBODY has also been used to develop a model of the satellite which takes into account the non-linear multi body dynamics, and it has been used to compare and asses the validity of the SDTlib model. Although this non-linear model can be linearized around a given configuration, it does not yield an LFT representation. As will be shown, simulations using this approach are significantly slower than those based on the LPV model.

Figure 11 shows a comparison of the (linearized) Simscape and SDTlib models in frequency domain, for the deployed configuration. As the figure shows, the models are equivalent in this configuration.

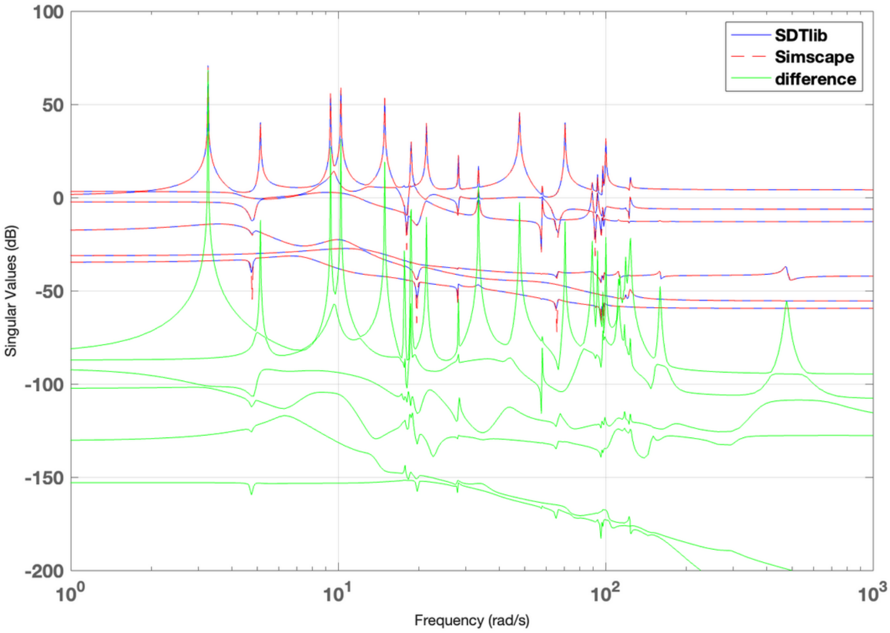

Fig. 11 Frequency-domain comparison between SDTlib and Simscape-Multibody models (and their difference)

Figure 12 shows the time-domain comparison of the two models, in particular the response of the axial load on the hinge between two booms during deployment. Notably, the computation time of the LPV simulation for the SDTlib model was 4s, against 700s for the non-linear simulation of Simscape on the same machine. A good agreement can be observed between the frequencies and magnitudes of the main oscillations. The remaining discrepancies are primarily attributed to differences in the modelling of local damping within the hinges.

The LPV simulations are detailed in the next sections.

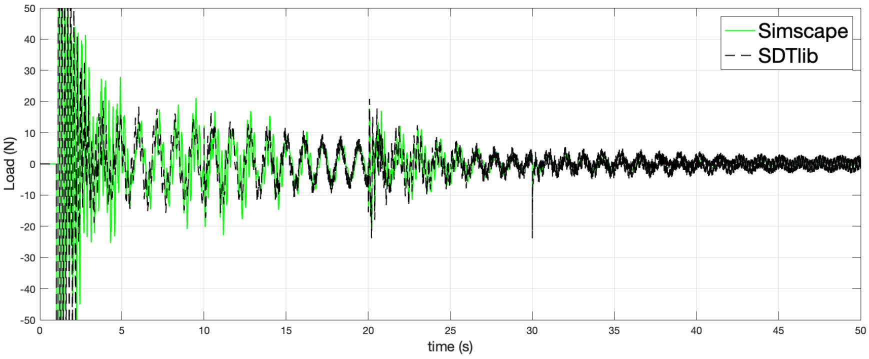

Fig. 12 Time-domain Simscape/SDTlib comparison: response of the axial load on the hinge between the 2 deployable booms during a 50 second (exaggeratedly) aggressive deployment (without AOCS).

4 Simulation environment

4.1 LPV - SDTlib model

Generally speaking, the simulation of multibody systems requires to solve the forward and the inverse dynamics, at each time step, to derive a nonlinear state-space equation of the form:

$$\dot{\boldsymbol{x}}(t) = f(\boldsymbol{x}(t), \boldsymbol{u}(t)) \tag{3}$$

that can be numerically integrated [11]. Although numerous methods exist to efficiently solve these two steps, it is generally computationally expensive. Flexible multibody systems lead to additional difficulties [12], and current commercial software such as Simscape-Multibody can be very slow to simulate them.

In this paper, it is proposed instead to perform LPV simulation of the spacecraft. The spacecraft model $\mathbf{D}_G(s, \boldsymbol{\Theta})$ corresponds to a linearization around the equilibrium trajectory $\dot{\boldsymbol{x}} = 0$, and can be written as the linear state-space:

$$\begin{cases} \dot{\boldsymbol{x}} = \boldsymbol{A}(\boldsymbol{\Theta})\boldsymbol{x} + \boldsymbol{B}(\boldsymbol{\Theta})\boldsymbol{u} \\ \boldsymbol{y} = \boldsymbol{C}(\boldsymbol{\Theta})\boldsymbol{x} + \boldsymbol{D}(\boldsymbol{\Theta})\boldsymbol{u} \end{cases} \tag{4}$$

that represents small variations around the equilibrium trajectory, a reasonable assumption given the time scale of the deployment. In other words, this model captures the variations of the spacecraft geometry during deployment, but neglects second-order terms in $\dot{\boldsymbol{\Theta}}^2$. With this model, it is no longer necessary to solve forward or inverse dynamics at each time step. The simulation becomes:

- Integrate the linear system (4) for the current $\boldsymbol{\Theta}(t)$, to obtain $\boldsymbol{x}(t + dt)$ and in particular $\boldsymbol{\Theta}(t + dt)$. We used SIMULINK default solver.
- Update the matrices $\boldsymbol{A}(\boldsymbol{\Theta}(t+dt))$, $\boldsymbol{B}(\boldsymbol{\Theta}(t+dt))$, $\boldsymbol{C}(\boldsymbol{\Theta}(t+dt))$, $\boldsymbol{D}(\boldsymbol{\Theta}(t+dt))$. However, to further improve computational speed, we only updated these matrices every 5s (simulation time).

It is important to remark that the model in equation (4) is derived analytically with the SDTlib, and continuously captures all parametric configurations. Indeed, each subsystem is defined directly from the physical equations, without resorting to interpolation or any other approximation method (apart from the linearity assumption).

4.2 Overview of the simulator

The deployment simulations are performed in a simplified linear environment, excluding sensors, actuators, and estimation dynamics. The only external perturbation considered is the gravity gradient, as it is most affected by the changes in the spacecraft's inertia, which are accounted for in the simulator and, as shown in Fig. 9, are significant during deployment. This setup is sufficient for the primary objective, namely to assess the performance of the LPV control strategy relative to a standard deployment control approach. Nevertheless, the SDTlib multibody framework is capable of handling more complex environmental scenarios, including the modelling of non-linear hinge behaviours such as detent torque, backlash, and viscous or dry friction.

Figure 13 shows the simulation environment schematic, the LPV - SDTlib model with its inputs/outputs detailed in the previous sections, the hinges deployment mechanism, the LPV controller K_{LPV} and the gravity gradient torque $\mathbf{T}_{GG}$. As it is shown in the scheme, the inertia matrix $\boldsymbol{J}_G(\boldsymbol{\Theta})$ of the satellite computed at point G, which depends on the geometric configuration vector $\boldsymbol{\Theta}$, is given at each time step from the LPV-satellite model and fed to the controller and gravity gradient torque blocks, as it will be detailed in the next sections.

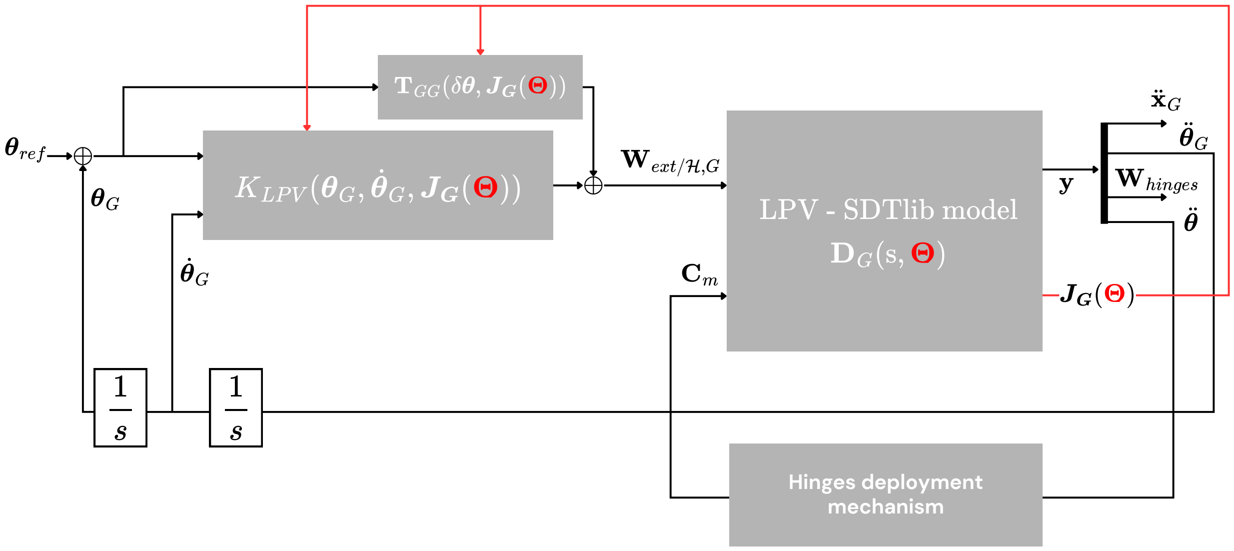

Fig. 13 Simulation environment schematic

4.3 Analytical LPV controller

The LPV controller block takes in input the attitude angles and rates $(\boldsymbol{\theta}_G, \dot{\boldsymbol{\theta}}_G)$ obtained from integrating the satellite angular acceleration output of the LPV model, as well as the time-varying inertia of the satellite which depends on the geometric configuration vector $\boldsymbol{\Theta}$. The plant consists of a PD controller combined with a first-order low-pass filter, designed to suppress unwanted high-frequency modes (whose exact characteristics are not well known). The resulting 3 × 1 control torque vector is:

$$\boldsymbol{\tau}_{LPV}(s, \boldsymbol{\Theta}) = [\boldsymbol{K}_p(\boldsymbol{\Theta})(\boldsymbol{\theta}_{ref} - \boldsymbol{\theta}_G) - \boldsymbol{K}_v(\boldsymbol{\Theta})s\boldsymbol{\theta}_G]F(s, \omega_c) \tag{5}$$

where $\boldsymbol{K}_p(\boldsymbol{\Theta}) = [K_p^x, K_p^y, K_p^z]^T(\boldsymbol{\Theta})$ and $\boldsymbol{K}_v(\boldsymbol{\Theta}) = [K_v^x, K_v^y, K_v^z]^T(\boldsymbol{\Theta})$ are defined as in Eq. 7, and $F(s, \omega_c)$ represents the first-order low pass filter with cut-off frequency ω_c:

$$F(s, \omega_c) = \frac{\omega_c}{s + \omega_c} \tag{6}$$

Two control modes are considered:

- **Safe mode** — characterized by a low controller bandwidth of $\omega = 0.01$ rad/s and a filter cut-off frequency of $\omega_c = 0.05$ rad/s. Its primary objective is to protect the unlatched hinges during deployment, even under failure scenarios, while maintaining limited pointing performance.
- **Normal mode** — with a higher controller bandwidth of $\omega = 0.1$ rad/s and a filter cut-off frequency of $\omega_c = 0.5$ rad/s.

As explained in Sec. 1, in the standard case the controller is disabled during the deployment phase and activated only once the mechanisms are latched. At this point, an initial safe control mode is employed, followed by the normal mode to restore pointing accuracy.

In contrast, under the LPV approach the safe control mode remains active throughout deployment, thereby reducing the attitude pointing error. After latching and with some delay (to account for failure scenarios), the controller switches to the higher-bandwidth mode to ensure accurate pointing performance. This strategy is enabled by explicitly accounting for the time-varying $\boldsymbol{J_G}(\boldsymbol{\Theta})$ and continuously adapting the PD gains in real time:

$$K_p^x(\boldsymbol{\Theta}) = \omega^2 J_G^{xx}(\boldsymbol{\Theta}), \qquad K_v^x(\boldsymbol{\Theta}) = 2\xi\, \omega J_G^{xx}(\boldsymbol{\Theta}). \tag{7}$$

where $\xi = 0.7$ is the damping ratio and J_G^{xx} is the first diagonal term of the inertia matrix $\boldsymbol{J_G}(\boldsymbol{\Theta})$. The same applies to $K_p^y, K_v^y, K_p^z, K_v^z$ with J_G^{yy} and J_G^{zz}.

The *analytical LPV controller* is valid throughout deployment if the hinge positions are perfectly known, as it can accommodate large variations in the inertia and center of mass. However, uncertainties in hinge angle measurements introduce a potential mismatch between the estimated and actual inertia matrices, in which case a robust approach becomes necessary. Although this controller is already tuned to limit hinge loads across all configurations, it does not explicitly account for parametric uncertainties such as flexible mode frequencies, delays, or misalignments. These aspects are deferred to the robust controller design. The analytical LPV controller nevertheless enables evaluation of deployment failures, AOCS equipment failures, and safe mode feasibility. It also provides a baseline for assessing pointing precision, hinge loads, and deployment duration. Finally, it is termed "analytical" since its tuning is based on bandwidth and filter considerations derived from analytical reasoning, without recourse to model-based optimization. While this simplicity allows rapid design, it may be conservative or insufficiently robust in the presence of parametric uncertainties or deployment anomalies.

4.4 Hinge Deployment Mechanism

This subsystem models the driving torque within the hinges during deployment. This torque is generated by a PD controller that drives the hinge angular configuration to follow the deployment reference. The latching mechanism is incorporated by modifying the controller stiffness and damping gains, as in Eq. 2 (with damping assumed to be 10 times smaller than stiffness).

It is worth noting that this PD controller is not part of the control strategy being tuned, but rather a modelling element introduced to reproduce the reaction torques acting at the hinges. This is necessary because the current multi body framework does not explicitly enforce conservation of angular momentum. In practice, this subsystem is considered part of the model itself, with fixed gains that are not subject to optimization or design.

4.5 Gravity Gradient Torque

Assuming the satellite is in a circular orbit at an altitude of 666 km (BIOMASS mission's altitude), and that the radial vector from the Earth's center to the satellite is aligned with the satellite's Z-axis in its body-fixed reference frame, the gravity gradient torque is considered as a torque disturbance applied at the center of mass of the whole spacecraft. Note that this torque depends on the varying matrix of inertia (which is captured by the SDT model), and can be seen as the sum of an equilibrium contribution and a linearized contribution which acts as a feedback on the attitude misalignments $\delta\boldsymbol{\theta} = \boldsymbol{\theta}_{ref} - \boldsymbol{\theta}_G$:

$$\mathbf{T}_{GG} = \frac{3\mu_\oplus}{r^3}\left[\begin{pmatrix}\delta\boldsymbol{\theta}_y\\ -\delta\boldsymbol{\theta}_x\\ 1\end{pmatrix} \times \boldsymbol{J_G}(\boldsymbol{\Theta})\begin{pmatrix}\delta\boldsymbol{\theta}_y\\ -\delta\boldsymbol{\theta}_x\\ 1\end{pmatrix}\right], \tag{8}$$

where $\mu_\oplus$ is the Earth's gravitational parameter and r is the distance of the satellite from the center of the Earth, which in the case of a circular orbit is simply:

$$r = r_\oplus + h \tag{9}$$

with $r_\oplus$ being the Earth's radius (6378 km) and h the orbit's altitude of 666 km.

5 Results

This section presents the results obtained using the simulator described in Section 4.2, following a progressive control design approach of increasing complexity. First, the standard AOCS strategy is presented in Section 5.1. Section 5.2 then introduces the analytical LPV controller, and Section 5.3 formulates the problem within the robust control framework and presents the associated results.

5.1 Standard AOCS strategy

Figure 14 shows the attitude error over the full deployment sequence under the standard AOCS strategy (see Section 1). As observed, the satellite attitude exhibits significant variations during each deployment phase.

Indeed, with the Attitude Control System (ACS) disabled, the attitude error evolution closely correlates with the variations in the satellite inertia during deployment, as visible in Figure 16. In the absence of significant external torques (ACS disabled), angular momentum is conserved, such that changes in the inertia tensor induce corresponding variations in angular velocity and rotation axis.

Once the ACS is reactivated (dotted lines labeled *boom/Reflector Deployed* in Figure 14), a low-bandwidth control mode is applied for approximately 9 minutes, after which the high-bandwidth mode reduces the attitude error to zero within about 3 minutes. The transition between the low- and high-bandwidth modes can be observed in the zoom box of Fig. 14.

The duration of each deployment step is selected to resemble that of the BIOMASS mission, while the intervals between steps (corresponding to the repointing phases) are shortened compared with real-life constraints, allowing the entire deployment to be represented within a single figure. This simplification does not affect the simulation of each deployment step, as sufficient time is still allowed for the system to reach convergence before proceeding to the next phase.

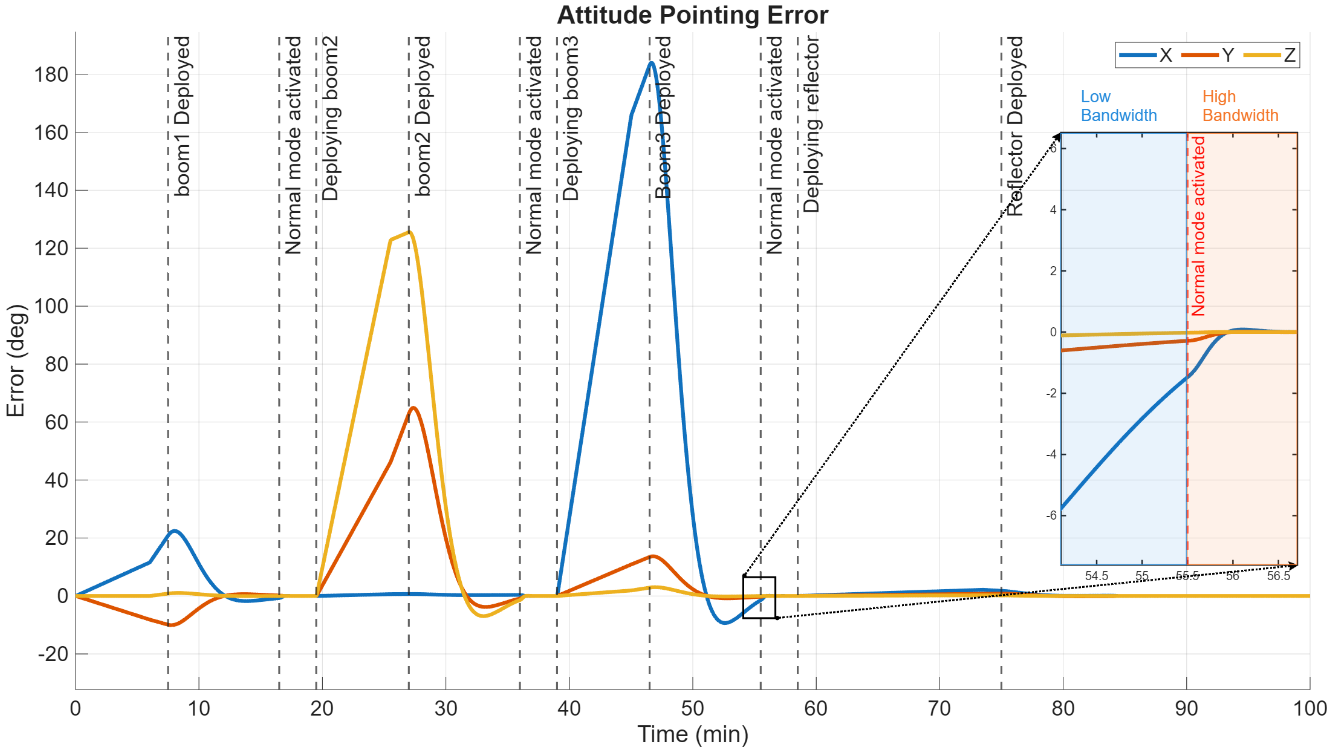

Fig. 14 Pointing error during deployment (standard AOCS strategy). AOCS is disabled during each deployment, safe mode is activated at end of deployment, and normal mode is activated a few minutes later (cf. zoom box)

The torques acting on the joints during the simulation are monitored as in Fig. 15. High torque peaks are observed during latching events, transitions between safe and nominal modes, the initiation of deployment phases, and instances of sudden inertia changes (as visible in Fig. 16). It is important to remark that these high torques values are not physical, as our latching model is extremely simplified. Rather, the interest of Fig. 15 is to highlight the capacity of the proposed framework to monitor the torques variations during each deployment step.

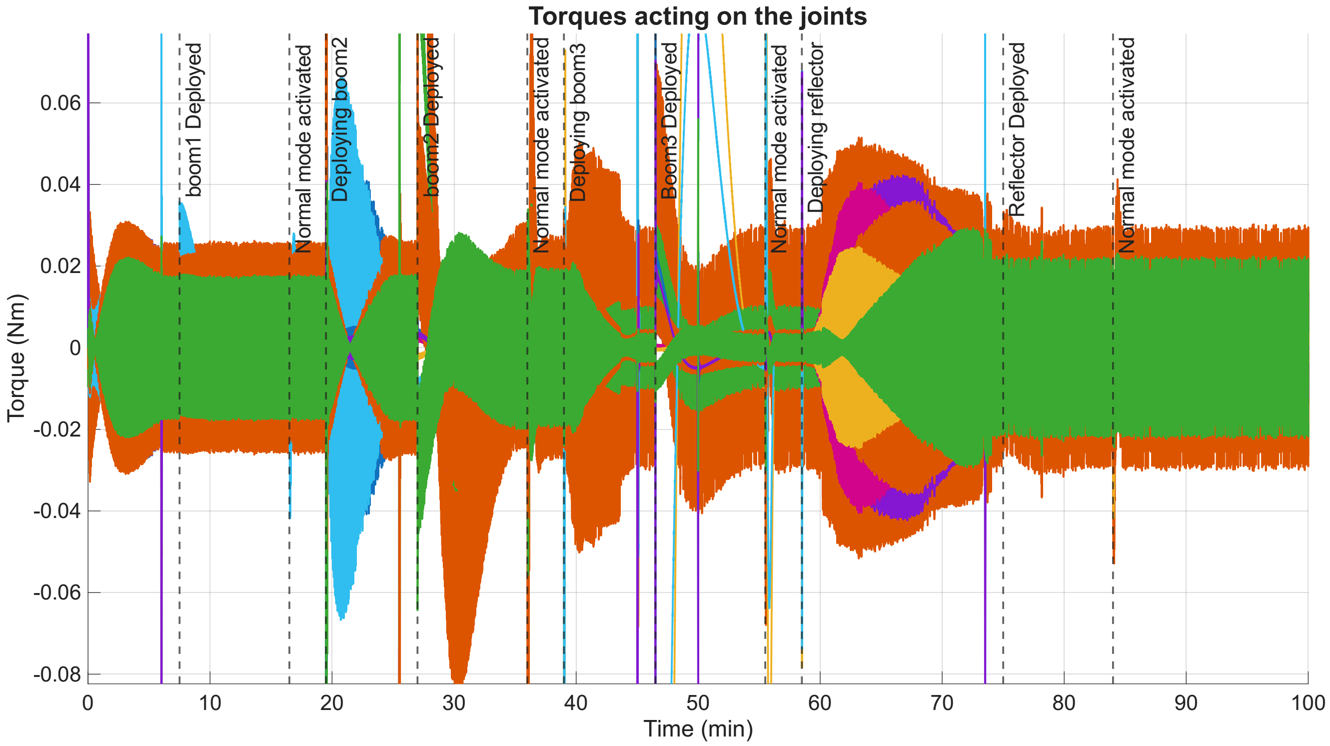

Fig. 15 Torques acting on the joints with the standard AOCS strategy

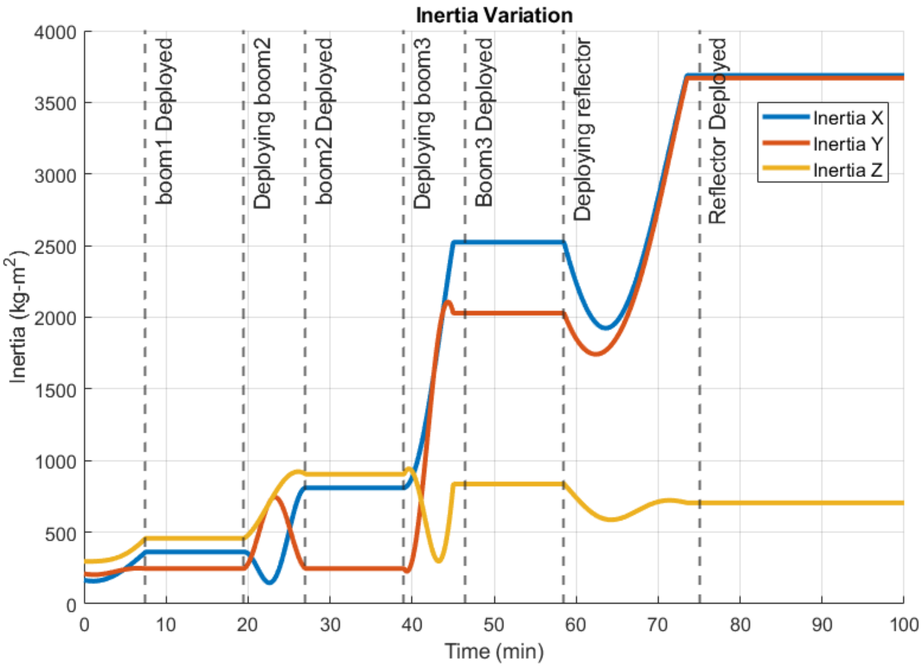

Fig. 16 Inertia tensor's diagonal terms variation during deployment in simulation environment

5.2 LPV control strategy

Figure 17 presents the full deployment simulation using the LPV control strategy. As observed, the LPV controller significantly reduces the pointing error compared to the standard AOCS strategy, with a maximum error along the X-axis of approximately 25°, versus about 181° with the previous approach.

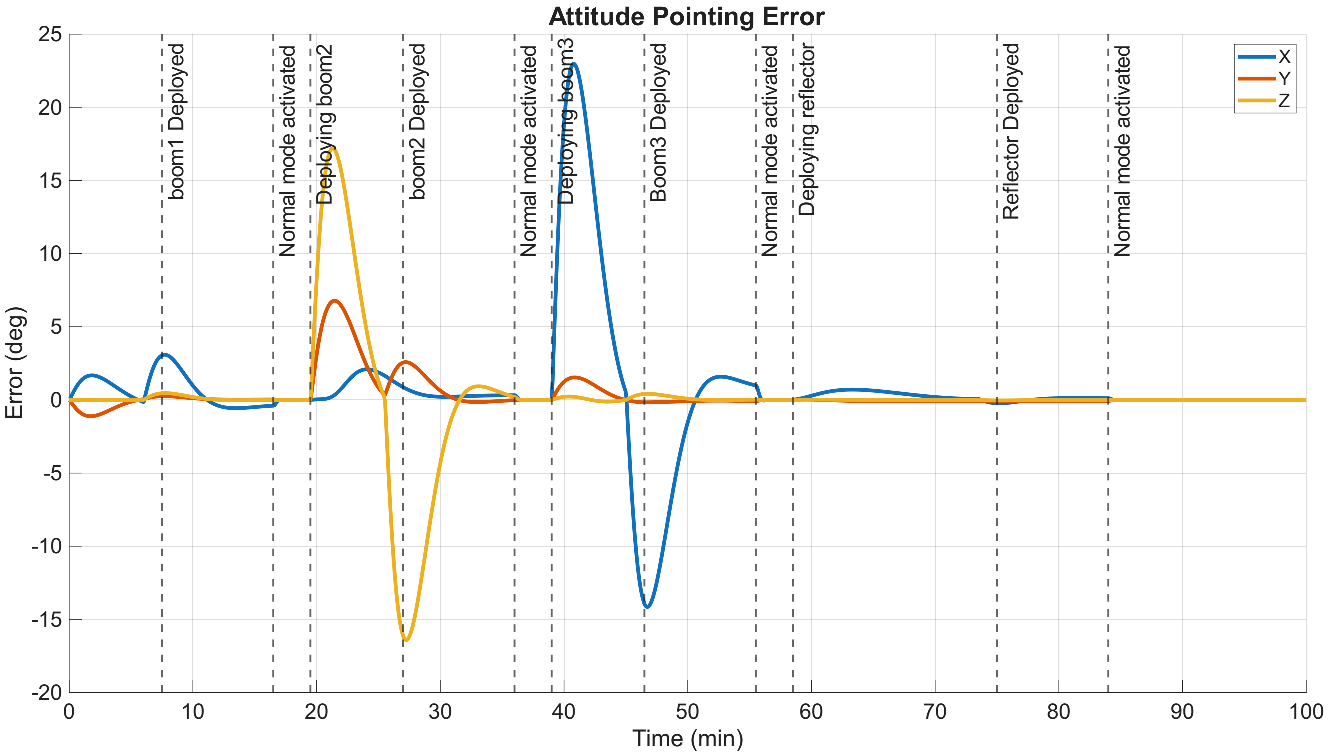

Fig. 17 Pointing error during deployment with the analytical LPV controller

Figure 18 shows the joint torques during the LPV-controlled deployment. While the attitude error exhibits significant improvements compared to the previous strategy, the torque magnitudes remain of the same order. However, as previously noted, these values should be interpreted with caution. A more meaningful comparison will be possible with future refinements of the latching mechanism model.

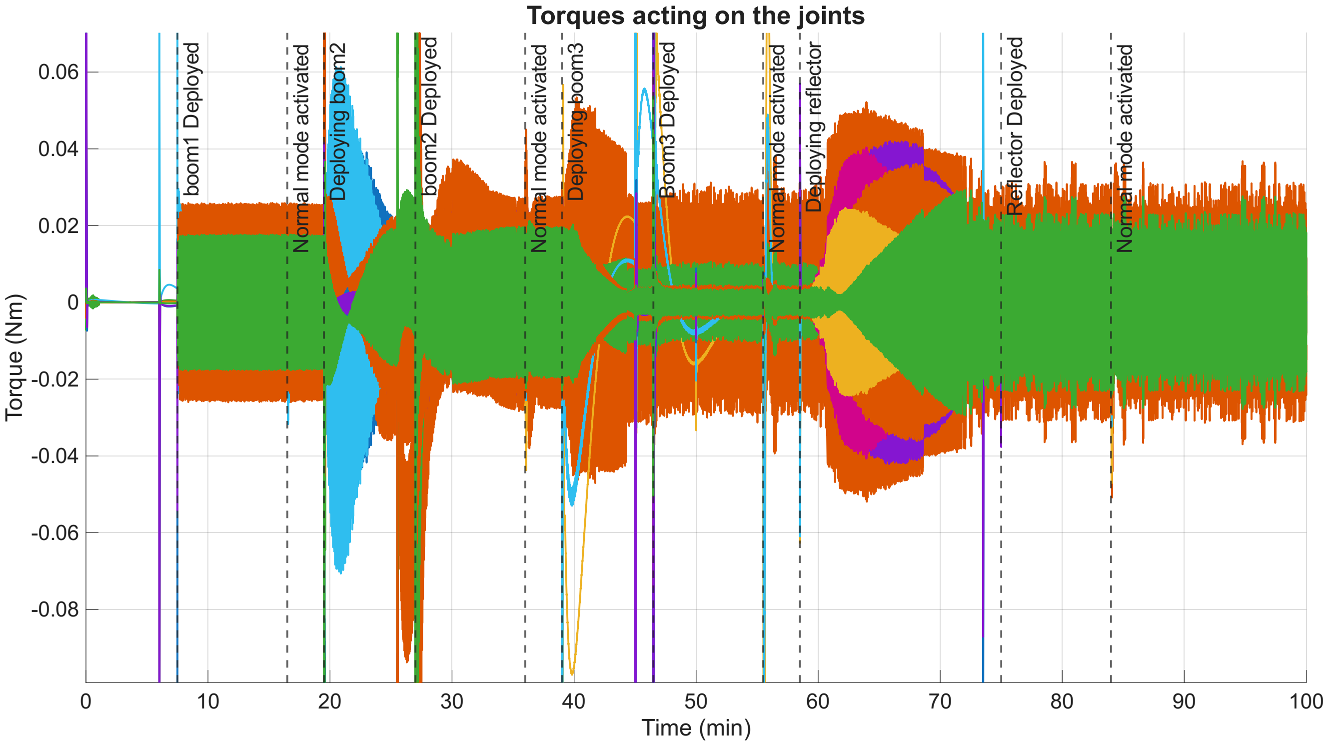

Fig. 18 Torques acting on the joints with the LPV control

5.3 Robust controller

As previously discussed, from a control perspective, the deployment of large appendages presents a significant challenge. The AOCS must be robust to a wide range of dynamic conditions, including variations in the center of mass, inertia properties, flexible modes, and external disturbances such as varying gravity gradient torques. Moreover, the control bandwidth must remain limited to prevent excessive rate variations and the excitation of the flexible modes in the appendages. These characteristics make the problem well-suited for robust control methodologies, which are designed to handle uncertain, multiple-input-multiple-output (MIMO) systems effectively.

In this section, the control problem is formulated within the robust control framework using the structured $\mathcal{H}_\infty$ technique [13]. The synthesis algorithm behind this technique is based on non-convex optimization, but its ease of use and the availability of consolidated design software tools have allowed it to become one of the preferred industrial control design techniques in the recent years. This technique has already been applied to real systems such as ESA's Rosetta [14], CNES' Microscope satellite [15], and the VEGA launcher [16], and has also been flight-tested in JAXA's fly-by-wire aircraft [17].

For this first iteration, only the initial deployment step is considered in order to assess the capabilities of the robust control framework for this specific control problem. During this stage, the principal inertia terms along x and z axes show a significant increase from the beginning to the end of the deployment, while the inertia along y axis exhibits comparatively minor variation (see Fig. 16).

An initial rigid-body design was performed to obtain a single PD controller that remains robust across the full range of the inertia values using the so-called multi-model design approach [18]. Similar to the analytical LPV controller case, a PD controller is combined with a fixed first-order low-pass filter aimed at attenuating high-frequency flexible modes. The design is posed using the structured $\mathcal{H}_\infty$ approach (via the *systune* algorithm) in a MIMO setting to synthesize a three-axis controller in a single procedure, explicitly accounting for the couplings introduced by cross-inertia terms.

The tuning objectives use sensitivity and complementary sensitivity functions to enforce a control bandwidth that remains well below the lowest bending frequency throughout the entire deployment step. Additionally, a weighting function was included to penalize actuation effort.

The results are shown in Fig. 19, alongside the analytical LPV controller responses for comparison. The results demonstrate that the proposed design achieves less overshoot and better overall tracking performance. Although not shown here, the design also produces torque levels comparable to those of the analytical solution.

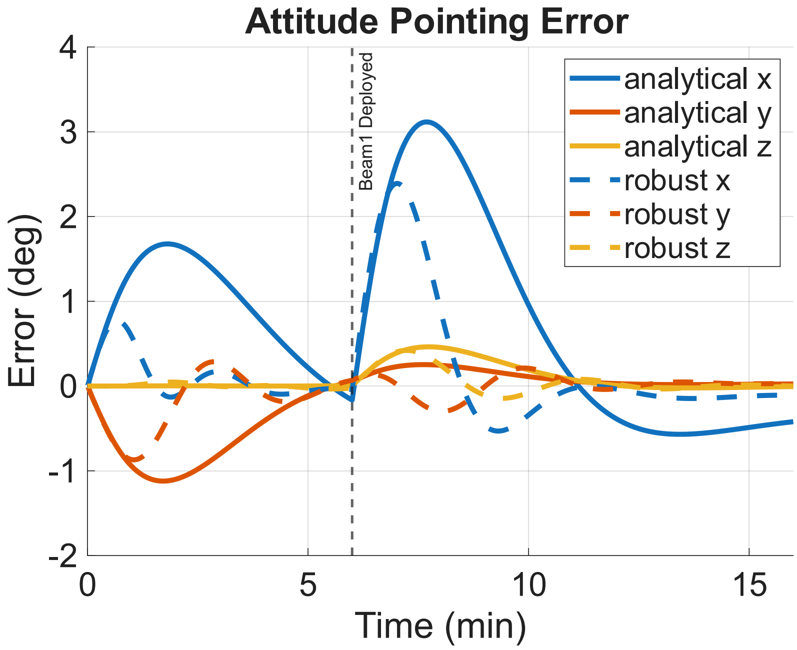

Fig. 19 Pointing error during first deployment with the robust controller

This performance improvement (achieved without modifying the controller structure) demonstrates the value of tailoring the design within the robust control framework. This work paves the way for future improvements, such as explicitly accounting for parametric uncertainties and incorporating external disturbances directly into the synthesis process.

Note that for this case, a single non-scheduled PD controller copes well with the range of inertia variation observed during the first deployment step. For subsequent deployment stages, gain scheduling may be required to handle further dynamic changes. Advantageously, the same framework used for this initial design can be naturally extended to explore self-scheduling approaches as well as pure LPV techniques.

6 Conclusions

This work presented a Linear Parameter Varying framework for continuous satellite attitude control during the deployment of large flexible appendages, applied to a spacecraft configuration inspired by the BIOMASS mission.

The satellite model was derived using the Satellite Dynamics Toolbox Library based on the TITOP multibody approach, yielding an LFT representation that captures all geometric and kinematic parameter variations within a single, analytically consistent plant model. The resulting LPV model was validated against a high-fidelity Simscape-Multibody nonlinear simulation in both frequency and time domains, offering a computational speedup of more than two orders of magnitude.

A preliminary deployment analysis confirmed that the spacecraft undergoes dramatic changes in inertia during deployment — up to a factor of twenty along the principal axes — alongside significant variations in flexible mode frequencies driven by hinge stiffness transitions between latched and unlatched states. These observations motivate the need for a control strategy that explicitly accounts for the time-varying nature of the plant throughout the deployment sequence.

The proposed analytical LPV controller, scheduled by the real-time inertia matrix, demonstrated a substantial reduction in attitude pointing error compared to the standard AOCS strategy: a maximum error of approximately 25° versus 181° along the X-axis, while maintaining control authority continuously throughout deployment without requiring ground updates between steps. This approach simplifies operations, reduces re-pointing durations, and offers a clear path toward safer and more efficient deployment for future missions.

Finally, an $\mathcal{H}_\infty$ robust LPV controller was developed for the first boom deployment phase, demonstrating stability and improved pointing performance across the full range of inertia variations encountered during that step. This result validates the suitability of the LFT-based modeling framework as a direct input to standard robust control synthesis tools, and confirms that a single controller can handle the plant variability associated with a deployment phase rather than requiring multiple mode-switched designs.

Several directions remain open for future work. The most immediate extension is to broaden the robust controller design to cover the complete deployment sequence, including all boom and reflector phases, which will require managing a larger parameter space and potentially more demanding robustness constraints. Incorporating parametric uncertainties on mechanical properties, such as flexible mode frequencies, mass and inertia properties, as well as realistic external disturbances beyond the gravity gradient, will further stress-test the framework and bring the simulation environment closer to operational conditions. Finally, a higher-fidelity model of the latching mechanism will enable a more physically meaningful evaluation of hinge load constraints throughout deployment, a critical requirement for the protection of fragile mechanisms and the qualification of future missions.

Declaration of Use of Artificial Intelligence

The authors acknowledge the use of an AI tool (ChatGPT: GPT-4/5) to assist in the reformulation of certain sentences.

References

[1] T. Pareaud et al. Gnc design solution for the deployment of biomass large deployable reflector. In *Proceedings of the ESA GNC 2020 Conference*. European Space Agency, 2020. `https://www.esa-gnc.eu/paper/?paper_id=1335`.

[2] Daniel Alazard and Francesco Sanfedino. Satellite dynamics toolbox for preliminary design phase. In *43rd Annual AAS Guidance and Control Conference, 30 January 2020 - 5 February 2020 (Brechenridge, United States)*, pages 1461–1472, 2020.

[3] Daniel Alazard and Francesco Sanfedino. Satellite dynamics toolbox & library. `https://personnel.isae-supaero.fr/daniel-alazard/matlab-packages/satellite-dynamics-toolbox.html`. Accessed: 2020-01-25.

[4] Jawhar Chebbi, Vincent Dubanchet, José Alvaro Perez-Gonzalez, and Daniel Alazard. Linear dynamics of flexible multibody systems: a system-based approach. *Multibody System Dynamics*, 41(1):75–100, 9 2017. ISSN: 1384-5640. doi: 10.1007/s11044-016-9559-y.

[5] F. Sanfedino, D. Alazard, A. Kiley, M. Watt, P. Simplicio, and F. Ankersen. Robust monolithic versus distributed control/structure co-optimization of flexible space systems in presence of parametric uncertainties. In *Proceedings of the ESA GNC 2023 Conference*. European Space Agency, 2023.

[6] F. Sanfedino, G. Thiébaud, D. Alazard, N. Guercio, and N. Deslaef. Advances in fine line-of-sight control for large space flexible structures. *Aerospace Science and Technology*, 130:107961, 2022.

[7] F. Sanfedino, D. Alazard, V. Preda, and D. Oddenino. Integrated modeling of microvibrations induced by solar array drive mechanism for worst-case end-to-end analysis and robust disturbance estimation. *Mechanical Systems and Signal Processing*, 163:108168, 2022.

[8] R. Rodrigues, V. Preda, F. Sanfedino, and D. Alazard. Modeling, robust control synthesis and worst-case analysis for an on-orbit servicing mission with large flexible spacecraft. *Aerospace Science and Technology*, page 107865, 2022.

[9] Vincent Dubanchet. *Modeling and control of a flexible space robot to capture a tumbling debris*. PhD thesis, Université de Montréal, 2016.

[10] A. Falcoz, M. Watt, M. Yu, A. Kron, P. P. Menon, D. Bates, and L. Massotti. Integrated control and structure design framework for spacecraft applied to biomass satellite. *IFAC Proceedings Volumes*, 46(19):13–18, 2013.

[11] Reinhold Schwerin. *MultiBody System SIMulation: Numerical Methods, Algorithms, and Software*. Springer Berlin Heidelberg, December 2012. ISBN: 978-3-642-58515-9, 978-3-540-65662-3. doi: 10.1007/978-3-642-58515-9.

[12] B. Rong, X. Rui, L. Tao, et al. Theoretical modeling and numerical solution methods for flexible multibody system dynamics. *Nonlinear Dynamics*, 98:1519–1553, 2019. doi: 10.1007/s11071-019-05191-3.

[13] Pierre Apkarian, Minh Ngoc Dao, and Dominikus Noll. Parametric robust structured control design. *IEEE Transactions on Automatic Control*, 60(7):1857–1869, 2015. doi: 10.1109/TAC.2015.2396644.

[14] Alexandre Falcoz, Christelle Pittet, Samir Bennani, Anne Guignard, Cedric Bayart, and Benoit Frapard. Systematic design methods of robust and structured controllers for satellites: Application to the refinement of rosetta's orbit controller. *CEAS Space Journal*, 7(3):319–334, June 2015. ISSN: 1868-2510. doi: 10.1007/s12567-015-0099-8.

[15] Christelle Pittet and Pascal Prieur. Structured accelero-stellar estimator for microscope drag-free mission. In Joël Bordeneuve-Guibé, Antoine Drouin, and Clément Roos, editors, *Advances in Aerospace Guidance, Navigation and Control*, pages 591–604, Cham, 2015. Springer International Publishing. ISBN: 978-3-319-17518-8.

[16] D. Navarro-Tapia, A. Marcos, P. Simplício, S. Bennani, and C. Roux. Legacy recovery and robust augmentation structured design for the vega launcher. *International Journal of Robust and Nonlinear Control*, 29(11):3363–3388, 2019. doi: https://doi.org/10.1002/rnc.4557.

[17] Andrés Marcos and Masayuki Sato. Flight testing of an structured h-infinity controller: An eu-japan collaborative experience. In *2017 IEEE Conference on Control Technology and Applications (CCTA)*, pages 2132–2137, 2017. doi: 10.1109/CCTA.2017.8062768.

[18] Pierre Apkarian, Pascal Gahinet, and Craig Buhr. Multi-model, multi-objective tuning of fixed-structure controllers. In *2014 European Control Conference (ECC)*, pages 856–861, 2014. doi: 10.1109/ECC.2014.6862200.